

Impact of distributed meteorological forcing on snow **cover and simulated hydrological fluxes over a mid-elevation alpine micro-scale catchment**

Aniket Gupta¹, Alix Reverdy¹, Jean-Martial Cohard¹, Didier Voisin¹, Basile Hector¹, Marc Descloîtres¹, Jean-Pierre Vandervaere¹, Catherine Coulaud¹, Romain Biron¹, Lucie Liger², Jean-Gabriel Valay², and Reed Maxwell³

¹Univ. Grenoble Alpes, CNRS, IRD, Institut des Géosciences de l'Environnement (IGE), UMR 5001, Grenoble, France

²Université Grenoble Alpes, CNRS, Lautaret, F-38000, Grenoble, France

³Department of Civil and Environmental Engineering, Princeton University, Princeton, NJ, USA

Correspondence: Aniket Gupta (aniket.gupta@univ-grenoble-alpes.fr)

Abstract. From the micro to mesoscale, water and energy budgets of mountainous catchments are largely driven by topographic features such as terrain orientation, slope, steepness, elevation together with associated meteorological forcings such as precipitation, solar radiation and **wind speed**. This **impacts** the snow deposition, melting and transport, which further impact the overall water cycle. However, this microscale variability is not well represented in Earth System Models due to coarse resolutions. **Moreover**, the impact of resolution on the simulated water and energy **balance** lacks quantification. **This study explores the impact of precipitation, shortwave radiation and wind speed on the water budgets over** a 15.28 ha small mid-elevation (2000-2200 m) alpine catchment at Col du Lautaret (France). The grass dominated catchment remains covered with snow for 5 to 6 months per year. The surface-subsurface coupled hyper-resolution (10 m) distributed hydrological model ParFLOW-CLM is used to simulate the impacts of meteorological variability at spatio-temporal micro-scale on the water cycle. **These include**

3D simulations of hydrological fluxes with spatially distributed forcing of precipitation, shortwave radiation and wind speed compared to 3D simulations of hydrological fluxes with non-distributed forcing. Our precipitation distribution method encapsulates the spatial snow distribution along with snow transport. The model simulates the dynamics and spatial variability of snow cover using the CLM energy balance module and under different combinations of distributed forcing. The resulting subsurface and surface water transfers are solved by the ParFLOW module. **Distributed forcing leads to spatially heterogeneous snow cover simulation, which becomes patchy at the end of the melt season and shows a good agreement with the remote sensing images (MBE = 0.22). This asynchronous melting results in a longer melting period compared to the non-distributed forcing, which does not generate any patchiness (MBE = 0.59, -0.4). Among the distributed meteorological forcings tested, precipitation distribution, including snow transport, has the greatest impact on spatial snow cover (MBE = 0.06) and runoff. Shortwave radiation distribution has an important impact on reducing evapotranspiration as a function of the slope orientation (decrease in regression slope from 1.55 to 1.18). For the primarily east-facing watershed studies, the distribution of shortwave radiation adds a small differential snowmelt with an increase in mean bias error (0.06 to 0.22) for all distributed forcing simulations compared to the simulation with only distributed precipitation. Distributing wind speed in the energy balance calculation has a more complicated impact on our catchment as it accelerates snowmelt when meteorological conditions are favourable but does not generate snow patches at the end of our test case.**

25 1 Introduction

Mountains are natural water reservoirs, which mitigate the variability of seasonal precipitation through snowpack accumulation. The gradual melting of the snowpack helps meet the demand for freshwater and energy all year long. The warmer climate expected in the near and far future for these regions will impact this mitigation process. Earth System Models (ESMs) are then challenged to simulate water fluxes in mountainous catchments. Highly variable mountain topography, vegetation, soils and geological structures **affect the water transfer** at different scales. In particular, topography controls precipitation estimation and uncertainties related to rain/snow partition, snow redistribution, slope/aspect effect and hill-shading that lead to spatial **differences in** melting (Costa et al., 2020; Fang and Pomeroy, 2020; Pomeroy et al., 2003, 2007). Fan et al. (2019) argued that variations in topography and catchment aspect can change **hydrological fluxes** and vegetation dynamics from steep to gentle

slope and from north to south aspect. Therefore, water budget modelling in the mountains is challenging, and the impacts of spatial heterogeneity, like snow depth distribution, calls for specific attention (Blöschl et al., 2019).

Land surface models (LSMs) are an imperative component of the ESMs to capture exchange of mass, energy and biogeochemical variables between the Earth surface and the atmosphere (Hurrell et al., 2013; van den Hurk et al., 2011). However, hydrological flux exchange between surface and subsurface in LSMs is often poorly constrained. Major approximations include free draining subsurface hydrology and coarse resolution with no specific subgrid parameterization. This could also include slope and aspects features (as hillshading) or meteorological subgrid variability (Clark et al., 2015; Fan et al., 2019) or underground horizontal water redistribution (Tran et al., 2020). The spatial variability of hydrological processes and associated variable flux responses are generally too fine to be represented in LSMs when used at several square km resolutions (Song et al., 2020). Bertoldi et al. (2014) mentioned that due to the lack of detailed subsurface characterization, they failed to simulate the heterogeneous soil moisture compared to observation over sloping terrains at 20 m resolution. Similarly, another study acknowledged that precipitation, solar insolation and wind speed distribution in a hillslope catchment are vital to simulate the spatial heterogeneity in surface hydrological fluxes and snow dynamics (Sun et al., 2018). Overall, the under representation of subgrid processes within mountain catchment controls the spatio-temporal snow cover, heterogeneous snow melting and resulting streamflow responses.

Differential snowmelt in a mid-elevation catchment leads to spatial variation in saturation and pressure head response which affects streamflow at the outlet. Loritz et al. (2021) mentioned the importance of the distribution of rainfall data over the catchment for spatial representation of surface and subsurface fluxes. The same study also highlighted that in a snow dominated catchment, the calibration of hydrological models should consider the surface dynamics of snow along with the runoff. Furthermore, evaluating the impact of snow redistribution by the wind over a catchment is challenging because it involves the hyper-resolution of wind vector (1 m to 100 m) to simulate snow transport in a mountainous catchment (Marsh et al., 2020; Pomeroy and Li, 2000). Liston et al. (2016) showed the relevance of the physical-statistical distribution of wind field in capturing snow dynamics. Similarly, shortwave radiation plays a significant role from a climatic, hydrologic and biogeochemistry point of view. Nijssen and Lettenmaier (1999) mentioned that shortwave radiation affects the majority of exchanges between land and the atmosphere. Land surface–radiation interactions rely on terrain, wind speed and soil moisture, and are often neglected in ESMs. Sampaio et al. (2021) highlighted that the daily/diurnal cycles of heat are also dependent on the surface orientation but merely taken into account in hydrological modeling. However, forcing distribution of single variable sometimes are not enough to capture the real catchment behaviour. Combining the terrain-based distribution of precipitation data with solar radiation and wind speed helps capturing differential snow melting along the slope, including distribution and redistribution of snow in the catchment (Sun et al., 2018). However, these diverse approaches in hydrological modeling are still limited and merely account for subsurface distribution, hyper-resolution simulation, terrain effect and surface meteorological variable distribution.

In mountainous regions it is hard to maintain a dense network of weather stations due to the complex terrain. (Meerveld et al., 2008; Revuelto et al., 2017; Song et al., 2020). This adds complexity to setting up hyper-resolution distributed models. However, there are proven statistical methods available for distributing the meteorological variables like precipitation, short-

70 wave radiation, wind speed, temperature and humidity over the catchment (Liston and Elder, 2006). Many studies focus only on accounting for temperature distributions in the forcings of the model to simulate the spatial variability of fluxes in snow-dominated hillslope catchments (Aguayo et al., 2020; Fang and Pomeroy, 2020). However, these model resolutions remain too coarse to simulate the micro-scale hydrological behaviour. Moreover, only few studies on snowpack simulation have used hyper-resolution distributed forcing (Günther et al., 2019; Baba et al., 2019; Vionnet et al., 2012). These studies highlighted the importance of meteorological distribution and need of hyper-resolution modeling framework. Yet, the practice of distributing multiple meteorological forcing in hyper-resolution hydrological modeling of mountainous catchments is limited.

In order to overcome these LSMs limitations and quantify the impacts of fine scale variability on water balance, we studied the impact of spatially distributed precipitation, wind speed and shortwave radiation on the hydrological budget in a unique modelling exercise using a small-scale alpine mid-elevation (2000-2200 m) catchment (15.28 ha) that can be investigated in details regarding surface and subsurface conditions. We have used a hyper resolution subsurface hydrological model (ParFLOW) coupled with the Common Land Model (CLM) at 10 m resolution to simulate the hydrological fluxes and spatio-temporal snow cover dynamics. From the perspective of hillslope hydrology we addressed the following points:

- Ability of the hyper-resolution modeling using 3D critical zone model ParFLOW-CLM to capture the water/energy fluxes in a sub-alpine snow-dominated catchment.
- Impact of precipitation, solar radiation and wind speed distribution over catchment; and its response in simulating the catchment hydrological fluxes.
- Snow cover spatio-temporal dynamics in a micro-scale catchment and its role in controlling the water budget.

From onward, the second section presents the study area location and its characteristics. The third section covers the methodology with details about the modeling framework. This section also includes details about the method to distribute the meteorological variables. The fourth section details the domain discretization and model setup. The fifth and sixth sections present the results and discussion, respectively. Finally, the seventh section conclude the study.

2 Study Area

2.1 Geography and geology

The study area lies in a mid-elevation range of sub-alpine region in the French Alps, close to the mountain pass, Col du Lautaret (Fig. 1). Being a micro-scale catchment, it covers 15.28 ha with elevation ranging between 2000 and 2200 m. It consists of steep slopes facing East in the upper area, and a wetland in the lower area. The catchment is covered by snow for 5 to 6 months per year. The warm season grassland dominates the summer with 5 % woody coverage that includes some larches, alders and bushes. Flux'Alp meteorological station lies just adjacent to the catchment (Fig. 1) in a flat zone. Over the catchment, soil depths range from 20 cm on steep slopes to more than 2 m on flat wetland. Soils are rich in clay with high porosity and retention capacity. This rich clay soil slowly transits to the hard rock towards the regolith up to 5 m at the deepest locations.

100 The base rock is highly fractured and made of “Flysch des Aiguilles d’Arves”, a shale-sandstone alternation, with bedding slopes ranging from sub-horizontal to sub-vertical (<https://infoterre.brgm.fr/>).

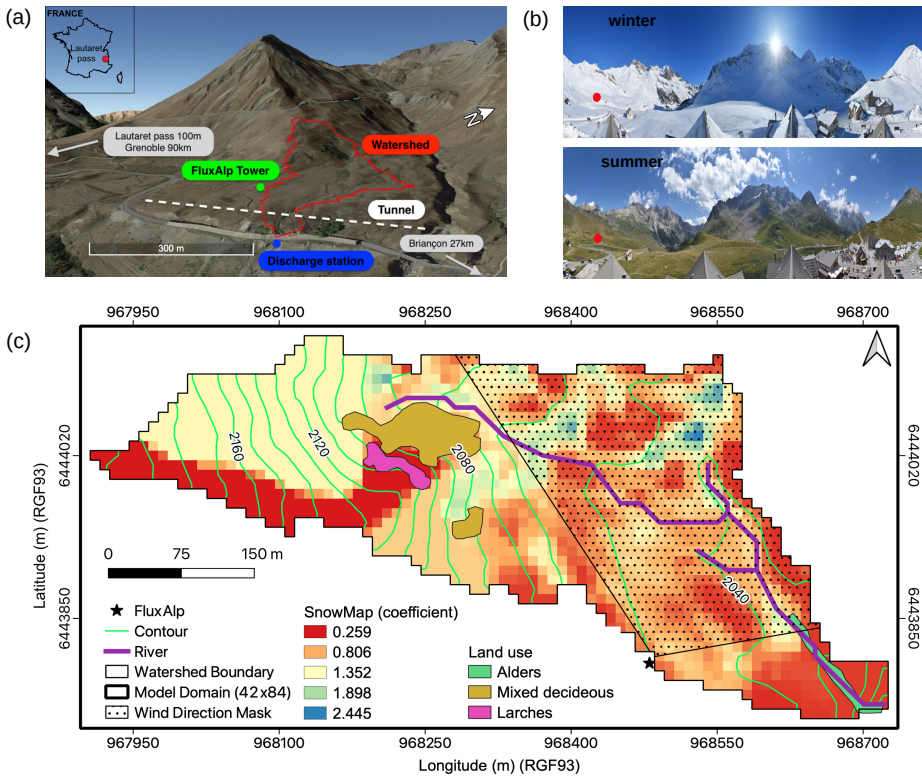


Figure 1. (a) overview of the study area at Col du Lautaret, France, the small sub-alpine catchment is delineated in red with the outlet at the blue point. Green dot (black star in 1(c)) is the Flux’Alp micro-meteorological station. (b) landscape views of the Lautaret pass area in winter (January) and summer (July). (c) Catchment domain (84 × 42 grid cells at 10 m resolution) with river branches (violet), elevation contours (green) and vegetation. Coloured pixels represent the distributed snow coefficients. The dotted area is the approximated footprint for the daily wind directions considered for ET comparison in (section 3.3).

2.2 Climate

The study area is located in a typical mid-latitude alpine climate. Figure 2 shows meteorological observations for the simulated hydrological year starting on 11 November 2017 at the first snowy day to 10 November 2018. The catchment has a long winter season with 5 to 6 months of snowfall (Fig. 2a) and snow cover. Flux’Alp meteorological station records a total of 1530 mm year⁻¹ precipitation, out of which 970 mm is snow (dry) in the studied period. According to 2017-2018 weather data, the site-average temperature is 4 °C. The site has below-zero winter conditions, with a -7.4 °C mean February temperature recorded and a 14 °C mean July temperature (Fig. 2b). Strong winds (Fig. 2c) are common throughout the year, usually from the South-West direction along the mountain pass (Fig. 4a). Temperature and specific humidity follows the same cyclic pattern (Fig. 2d).

110 March is the most humid period of the year, while July is the driest. The studied catchment has significant differences between summer and winter solar radiation (Fig. 2f). Additionally, mountains around the catchment reduces the sunshine period with projected shadow, especially during winter. **These observations time series are used as the input to force the model.**

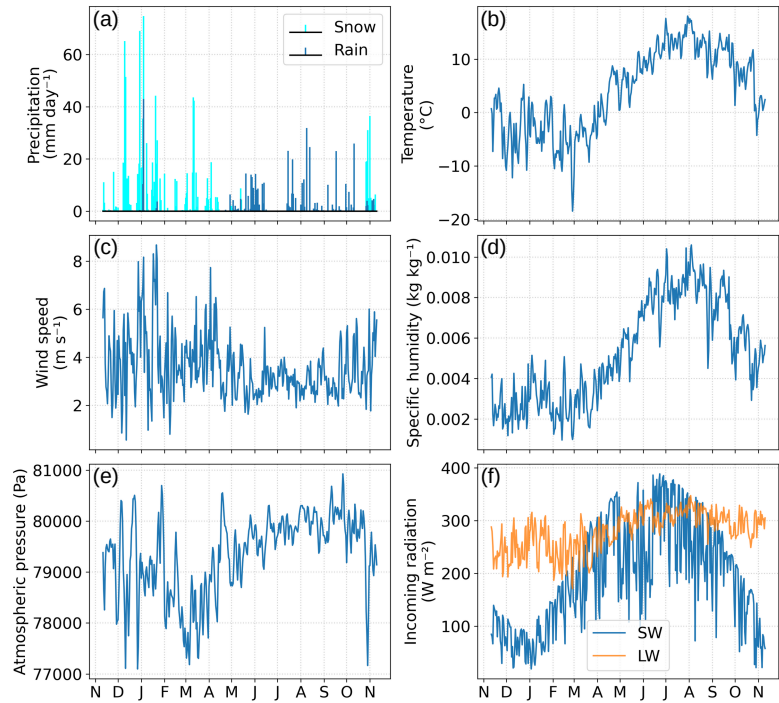


Figure 2. Daily meteorological observation at Col du Lautaret for hydrological year 2017-2018: precipitations (a), air temperature (b), wind speed (c), specific humidity (d), Atmospheric pressure (e) and shortwave (SW) and longwave (LW) incoming radiations (f).

2.3 Monitoring

Most of the monitoring on the site has started in 2012. It includes the temperature and humidity (CS215, Campbell Sc.), atmospheric pressure (Setra CS100, Campbell Sc.), **wind speed** and wind direction (Vector anemometer A100LK and W200P, Campbell Sc.), 4 components of net radiation (CNR4, Kipp and Zonen), snow height (SR50A, Campbell Sc.), and NDVI (Normalised Difference Vegetation Index) measured through Skye Instruments SKR1800. Since 2015, the site received eddy covariance sensors composed of the LI-COR LI-7200 close-path gas analyser and the HS50 Gill 3D sonic anemometer. **In 2017 an OTT Pluvio rain gauge was installed at the Flux'Alp weather station.** Site setup, monitoring and data processing follows the ICOS (<https://www.icos-ri.eu/>) standards, and the site has entered in this program since 2020. **All measured variables are recorded at 15 min time step and then upscaled to a 30 min mean time series (sum for precipitation) for this study.** The EddyPro Software **was** used to process the turbulent fluxes at the same 30 min time step following the ICOS recommendations (Hellström et al., 2016).

3 Methodology

125 3.1 ParFLOW-CLM (PF-CLM)

In this study, we have used ParFLOW-CLM, an integrated surface-subsurface coupled hydrological model, to simulate the impact of distributed meteorological forcing on the water transfers (Jones and Woodward, 2001; Ashby and Falgout, 1996; Kollet and Maxwell, 2006; Maxwell, 2013; Maxwell and Miller, 2005; Kollet and Maxwell, 2008). ParFLOW is a parallel integrated hydrological model optimised to solve the surface and subsurface exchange of fluxes. ParFLOW solves the three-dimensional Richards equation to calculate the water pressure field and transfer of fluxes between unsaturated and saturated porous media (Jefferson and Maxwell, 2015). Relative permeability and soil retention curves are based on the Van Genuchten relationships (Van Genuchten, 1980). A multigrid-preconditioned conjugate gradient solver and the Newton-Krylov solver for non-linear equations (Kuffour et al., 2020) make the model efficient to run on parallel computing environment. ParFLOW includes a terrain-following grid which eases boundary conditions prescription. It accounts the surface slope in the Darcy's formula which also eases numerical exchange between subsurface and overland flow. At the model surface, excess of water ($pressure > P_{atm}$) in all saturated cell flows according to the two-dimensional kinematic wave equation (Kuffour et al., 2020). ParFLOW then maintains a continuous pressure head value from the bottom to the top of the domain and explicitly calculates fluxes between ground water and surface water. Infiltration excess (Horton, 1933) or saturation excess (Dunne, 1983) runoff are then generated according to Richards equations. Flow-routing uses the D4 scheme to determine the flow direction based on individual slopes in x and y direction and has been calculated according to Condon and Maxwell (2019). The CLM (Common land model) is a land surface model designed to compute the land-water-energy exchange between the Earth's surface and atmosphere (Dai et al., 2003). CLM accounts for land cover, surface temperature, soil moisture, soil texture, soil colour, root depth, leaf and stem area, roughness length, displacement height, plant physiology and thermal and optical properties of medium to calculate the surface energy and water balance. It calculates evapotranspiration as the sum of evaporation, vegetation evaporation, transpiration and re-condensation. It also includes a five adaptive layer snow scheme to predict mass of water, mass of ice, layer thickness and temperature as main driving variables. CLM two-stream radiative transfer scheme accounts for direct and scattered radiation by snow in visible and near infrared wavelengths. In CLM, when pixels cover a large range of elevation, snow fraction is used to calculate the total snow cover area. In our study snow fraction was assigned to 0 (no-snow) or 1 (snow) values. Our horizontal pixel resolution is small enough (10×10 m) that we consider their snow cover to be uniform. This implies that either our pixels are completely covered with snow or they are bare. Therefore, CLM can handle the spatial/temporal snow distribution, associated water fluxes (melting, sublimation, infiltration) and evaporative fluxes according to spatial/temporal heterogeneous surface conditions (temperature, water/snow inputs, incoming radiations, wind speed and vegetation). After computing the surface exchanges like evaporation, transpiration, snowmelt and precipitation infiltration to and out of the soil, these are applied as source/sink in the Richards equations. Further information on ParFLOW terminology and the model capability is included in the user manual (<https://github.com/parflow>).

3.2 Meteorological distribution

3.2.1 Precipitation

The precipitation data from the rain gauge has been first processed to account for the lack of gauge shield (Klok et al., 2001). The adopted algorithm follows as:

$$160 \quad P_{corr}(x_0, y_0) = P(x_0, y_0) * (a + b * u(x_0, y_0)) \quad (1)$$

where, P_{corr} is the corrected precipitation (mm), P is measured precipitation (mm) at observation station, u is the wind speed at observation station in $m s^{-1}$, a and b are correction factors, and are different for rain ($a = 1.04$, $b = 0.04$) and snow ($a = 1.18$, $b = 0.20$) (Sevruk and WMO, 1986).

To account for snow cover spatial variability on the catchment domain, $S_c(x, y)$, the snow precipitation at (x, y) location
165 was calculated using a snow coefficient map $C_s(x, y)$. The snow coefficient map was prepared from the ratio between the measured snow height at the gauge to the snow height measured through the laser scan on the same day (21/02/2018) at the end of the accumulation period (Fig. 1). The snow height was calculated from the laser which basically is the difference of apparent snow height (from laser scan) at the end of the accumulation period and the digital elevation model (DEM) for the surface without snow. The snow DEM and surface DEM were prepared at the resolution of 2 m and were upscaled to 10 m
170 resolution using the nearest neighbour algorithm for modeling purpose. The $S_c(x, y)$ calculation hypothesizes that distributed snow cover on that date aggregates all spatial heterogeneity of the snow deposition including snow transport (redistribution). It also includes the snow compaction between date of deposition and the laser scan. Then the corrected Snow precipitation was calculated according to:

$$S_c(x, y) = S_m(x_0, y_0) * C_s(x, y) \quad (2)$$

175 where, $S_m(x, y)$ is the measured snow precipitation at the observation station. It must be noted that the laser scan didn't cover the upper part of the catchment. Zones not covered by the scanner were each given a fixed value according to our field observation. Moreover, due to micro-scale catchment and a low altitudinal range (1993 m to 2204 m), rain gradient between upper and lower altitude have not been considered and the rain has not been distributed in our study.

3.2.2 Shortwave radiation

180 The shortwave radiation, $SW_c(x, y)$ has been distributed from the observed shortwave radiation measurement, $SW_m(x_0, y_0)$ at the meteorological station considering the sun position and the terrain effect (Liston and Elder, 2006). Equation 3 partitions diffuse (30 %) and direct shortwave radiation (70 %) contributions from the observed shortwave radiation, and equation 4 accounts for the terrain features based on their orientation which was integrated as a solar cosine function in equation 3. The partition of diffuse and direct shortwave radiation was taken from the CLM technical setup (Oleson et al., 2004).

$$185 \quad SW_c(x, y) = (0.7 \cos i(x, y) + 0.3) * SW_m(x_0, y_0) \quad (3)$$

$$\cos i(x, y) = \cos \beta(x, y) * \cos Z(x, y) + \sin \beta(x, y) * \sin Z(x, y) * \cos(\mu(x, y) - \xi_s(x, y)) \quad (4)$$

SW_c is the corrected **shortwave radiation** (W m^{-2}) at a coordinate location, SW_m is measured **shortwave radiation** at the observation station, i is the solar angle function of the slope angle β , the slope southern azimuth ξ_s , sun southern azimuth μ and solar zenith angle Z .

190 3.2.3 Wind speed

Wind speed **was** spatialized to better account for the estimation of turbulent fluxes (Liston and Elder, 2006). The wind speed was distributed as,

$$W_w(x, y) = 1 + 0.58\Omega_s(x, y) + 0.42\Omega_c(x, y) \quad (5)$$

$$\Omega_s(x, y) = \beta(x, y) * \cos(\theta(x, y) - \xi(x, y)) \quad (6)$$

$$195 \quad \Omega_c(x, y) = 0.25 \sum (Z(x, y) - 0.5(Z_i(x, y) + Z_j(x, y))) / d \quad (7)$$

$$W_c(x, y) = W_w(x, y) * W_m(x_0, y_0) \quad (8)$$

where, W_w is the wind weighting factor at a coordinate location as function of wind direction slope (Ω_s) and curvature (Ω_c), i and j are the search direction (N-S, E-W, NE-SW, SE-NW), d is 2η for cardinal axes and $2\sqrt{2}\eta$ for others, η is the search distance and, Z is the elevation, β is the slope angle, θ is the wind direction and ξ is the slope azimuth. The search distance d for curvature was set to 50 m (Revuelto et al., 2020). Finally, the wind weighting factor (W_w) was multiplied with the **wind speed** measured (m s^{-1}) at observation station (W_m) to obtain the terrain corrected **wind speed** (W_c).

Along with precipitation, **shortwave radiation** and **wind speed**, three more variables are used to force the model: temperature, pressure and specific humidity. However, as the model was set to a micro-scale catchment with little altitudinal variability, we did not distribute these parameters.

205 3.3 Wind direction mask

To compare simulated evapotranspiration with observation, a wind direction mask was prepared to approximately represent the Eddy-Covariance station footprint area. As we only simulate a small catchment, actual footprint is sometimes not included in the limits of the catchment. To overcome this problem we have selected simulated pixels in an approximated footprint area based on a wind direction mask (Fig. 1) and averaged simulated values over the mask. The wind direction mask was prepared according to the prevailing wind directions towards the Flux'Alp station between 10 percentile (122.39°) and 90 percentile (260.51°) wind direction. We assumed that when wind blows towards this direction there is an enhanced similarity between observed and simulated evapotranspiration.

3.4 Sentinel-2 snow cover

Snowmelt dynamics was compared to Sentinel-2A and Sentinel-2B products from Sentinel-2 mission developed by European Space Agency (ESA) for high resolution satellite imagery (Drusch et al., 2012). We have downloaded four Sentinel-2 images out of which two belong to the accumulation period and two belong to the melting period. These images were selected to

show the spatial and temporal distribution of snow in the catchment. For this purpose we have calculated the normalised snow difference index (NDSI) from the downloaded images as (Dozier, 1989),

$$NDSI = \frac{Green(band3) - SWIR(band11)}{Green(band3) + SWIR(band11)} \quad (9)$$

220 where 'Green' and 'SWIR' are the corresponding bands in green and shortwave infrared region of the satellite, respectively. The green band is represented by 'band 3' and the SWIR band is represented by 'band 11' in Sentinel-2 product. The Sentinel-2 snow pixels were selected with $NDSI > 0.4$ (Riggs et al., 1994). In the model, the snow pixels were selected for snow depth threshold over 1 cm.

4 Domain discretization and simulation setup

225 The surface domain of 15.28 ha was discretized at a hyper-resolution of 10 m with the total number of $84 \times 42 \times 11$ (longitude \times latitude \times levels) cells on a terrain following grid (Fig. 1). As mentioned earlier, the model was mainly built and forced using the observations; hence, the input data either belongs to observation data or secondary data derived from observation. These data include the temperature, precipitation, wind speed, short wave, humidity and atmospheric pressure plotted on figure 2. These observations data were available at 30 minutes interval from the instruments. The data which were available at a higher
230 temporal resolution were upscaled to the 30 minutes temporal resolution using mean and sum approach. Leaf Area Index (LAI) and Stem Area Index (SAI) were calculated from NDVI measurements. Displacement height (d) and roughness length (z0) were calculated from the vegetation height following Brutsaert rules (Brutsaert, 1982). Grass height was calculated from the snow height sensor during the summer months considering NDVI to identify the vegetation/snow periods. LiDAR Digital Surface Model (DSM) of 2 m resolution was available for the catchment and upscaled to 10 m resolution for various elevation
235 related parametrization in the model. Upscaled DSM has been processed with PriorityFLOW to generate the slope maps in x and y direction (Condon and Maxwell, 2019). Landcover map was made through field observations while the Manning coefficients were assigned using the landcover map. The lateral and bottom boundary conditions were set to no flow and the surface boundary condition was at atmospheric pressure condition that allows surface runoff (Kollet and Maxwell, 2006). Hence, the inflow and outflow were restricted to exchange only through the surface. Subsurface has been made heterogeneous
240 with three layers consisting of soil, regolith and flysch which were divided into 11 numerical cells (Fig. 3a). The bottom of the domain was set deep enough to accommodate various subsurface water transfers (118 m deep from the surface). The soil physical parameters used in this study include porosity, permeability, soil horizons and Van Genuchten parameters. The curves are plotted on Fig. 3c, d for the three different horizons. They show a reduction of permeability and porosity with depth. Soil horizons distribution (Fig. 3b) were determined from an electromagnetic survey measuring apparent electrical conductivity
245 (related to water and clay content) and ground penetrating radar (GPR) measuring soil thickness. Electromagnetic survey has been done for the whole catchment however, GPR survey has been performed for three transverse profiles across the stream to validate the electromagnetic survey. The soil properties were determined by field permeability experiments and laboratory mercury porosity experiments. Elaboration about the detailed hydro-geological characterization is beyond the scope of this

study and will be detailed in a companion paper (Gupta et al., 2022, in preparation). This study is more focused on surface
 250 dynamics due to **surface meteorological variable distribution**.

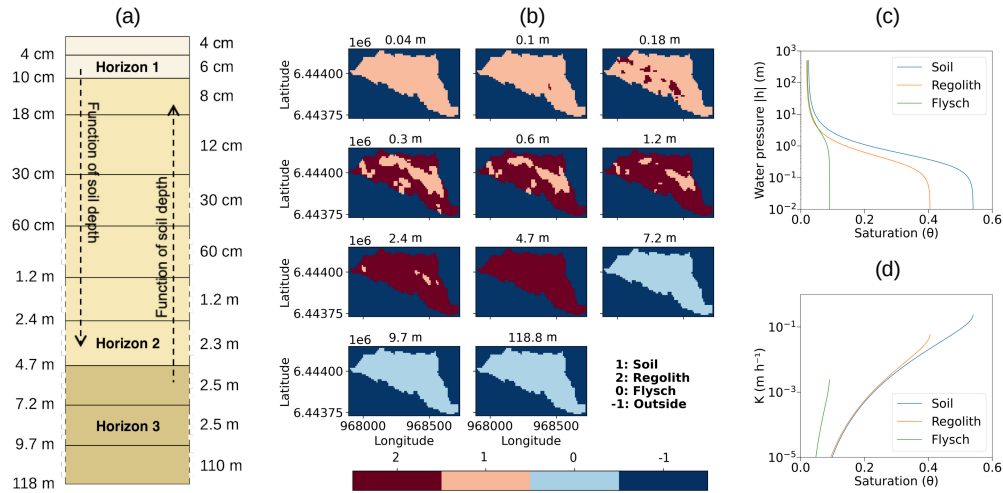


Figure 3. Subsurface configuration used for discretizing the domain. (a) The vertical distribution of subsurface layer with thickness (right) and depth (left) of each grid cell. (b) Spatial distribution of subsurface layer including soil (pink), regolith (dark brown) and flysch (blue). These layers vary in their hydro-geological parameters e.g. in terms of conductivity, porosity to the soil transfer functions which are shown in (c- Soil retention curve) and (d- hydraulic conductivity curve).

The model has been forced with half-hourly meteorological forcing, however results were written at hourly time-step. The Universal Time Zone (UTC) was considered in terms of monitoring and modeling for this study. Before running the actual simulations, a 10-years spin-up with ‘SeepageFace’ (no runoff) conditions was performed to bring the model into a hydrological balance. The yearly subsurface storage difference is used as spin-up parameter which reached the equilibrium in the end of
 255 the 10th year.

The different simulations setup for this study include:

- 1-dimensional column simulation of only precipitation distributed mean forcing (Pix-PM)
- 3-dimensional simulation of only precipitation distributed mean forcing (1D-PM)
- 3-dimensional simulation of all distributed mean forcing (1D-AM)
- 260 – 3-dimensional simulation of all distributed forcing (2D-AD)
- 3-dimensional simulation of only precipitation distributed forcing (2D-PD)
- 3-dimensional simulation of only shortwave radiation distributed forcing (2D-SD)
- 3-dimensional simulation of only wind speed distributed forcing (2D-WD)

	Precipitation	Shortwave radiation	Wind speed
Pix-PM	Distributed mean	Non-distributed	Non-distributed
1D-PM	Distributed mean	Non-distributed	Non-distributed
1D-AM	Distributed mean	Distributed mean	Distributed mean
2D-AD	Distributed	Distributed	Distributed
2D-PD	Distributed	Non-distributed	Non-distributed
2D-SD	Distributed mean	Distributed	Non-distributed
2D-WD	Distributed mean	Non-distributed	Distributed

Table 1. Distributed and non-distributed approach adopted for different simulation.

All simulations named 1D are the simulations with non-distributed forcing (Table 1). Rain is the major hydrological model input hence, we keep the same amount of precipitation input in all simulations (1443.72 mm), which corresponds to the spatial average of precipitation after applying the distribution formulae (eq. 2). Precipitation is reduced compared to what is measured at the rain gauge station (1531.96 mm) because the precipitation distribution process leads to a non-conservative spatial snow distribution over the catchment. This lead us to easily see the partitioning between different hydrological fluxes among separate meteorological forcing simulations. Similarly, shortwave radiation amount is not the same considering the measured value (averaged shortwave radiation: 190.8 W m^{-2}) and the distributed value when taking into account the slope angles (152.1 W m^{-2}). The shortwave radiation distribution scheme accounts for the slope hence, the shortwave radiation on average is reduced. For shortwave radiation forcing, we did several simulations to better analyse the results. Pix-PM, 1D-PM, 2D-PD and 2D-WD are run with the zenithal solar radiation observation (measured shortwave radiation) directly from the radiation sensor, and 2D-AD and 2D-SD are run with distributed solar radiation according to equation 5-8. The average of the distributed shortwave radiation is used to force the 1D-AM simulation (Table 1). 1D-PM corresponds to a classical hydrological simulation for small catchment when one applies the meteorological forcing directly from a nearby weather station. The latter four proposed simulations have been run to quantify the effect of spatially distributed forcing all together or individually.

Meteorological distribution algorithms described in section 3.2 aims at representing the slope, curvature and aspect effect in the spatial distribution. Fig. 4 presents snapshots of heterogeneities produced by these algorithms . Even at a micro-scale, one can observe the spatial meteorological variability along the grid after applying equation 2-8. In Fig. 4b, for an averaged 0.53 mm snow rate, the distribution algorithm produces large heterogeneities ranging from 0.2 mm to 1.2 mm. Deeper accumulation is mainly on low lands. Similarly for shortwave radiation (Fig. 4c) for an input radiation of 400.8 W m^{-2} on November 11 at noon, the algorithm reduces the radiation to 349.7 W m^{-2} on average with more than (+/-) 50 W m^{-2} depending on the location. In wind speed distribution, there is not so much variation in the spatial mean before and after wind speed distribution. The mean wind speed before and after the spatial distribution is 5.6 m s^{-1} and 5 m s^{-1} , respectively (Fig. 4d).

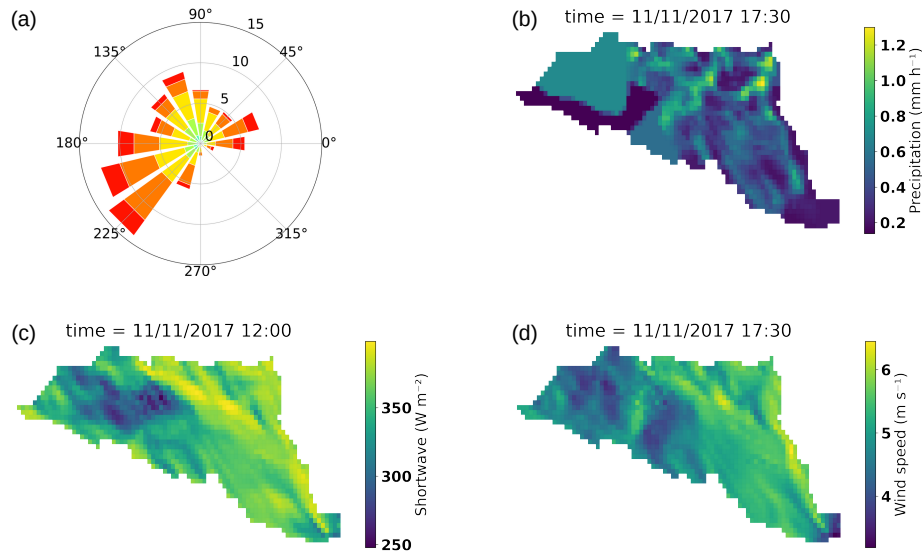


Figure 4. (a) Windrose diagram. (b) Precipitation distribution along the catchment. (c) Shortwave radiation distribution over the catchment. (d) Wind speed distribution over the catchment. All are plotted for the 11/11/2017 at 5:30 pm and 12:00 pm for shortwave radiation.

5 Results

5.1 Non-distributed forcing simulation

Figure 5a, b shows the catchment response from the 1D-PM for a full hydrological year and the monthly budgets for storage variation, surface and subsurface fluxes. It shows that the hydrological year begins with the snow accumulation period until the end of March. December and January are the snowiest months. Some snowmelt events (magenta line) can be observed during this period because of short above zero degree episodes (Fig. 2b) but generate very little runoff (black line). In April, continuous melting is simulated because of warmer positive temperature (Fig. 2b) but also rain on snow events. This produces the highest river discharge peaks on the hydrograph which follow the daily cycle (between min and max discharge values at daily timestep) and the rain timing (highest discharge peaks). This period also increases the subsurface storage (Fig. 5b) which produces a base flow that combines with the snowmelt contribution to the streamflow.

One of the most important and noticeable point while using the non-distributed forcing is the sudden disappearance of the snow at the end of the snowmelt season, which is usually not observed on actual field. This means that all the pixels behaved in the same way and there is no noticeable impact on the subsurface hydrology of the catchment spatial snow variability when considering a uniform forcing. From June to the beginning of the next snow period, summer rain produces almost instantaneous river responses and subsurface storage sustains stream discharge for several months. During this period, one can note a radical change of net radiation because of the change of the albedo from snow cover to herbaceous. The net radiation contributes to

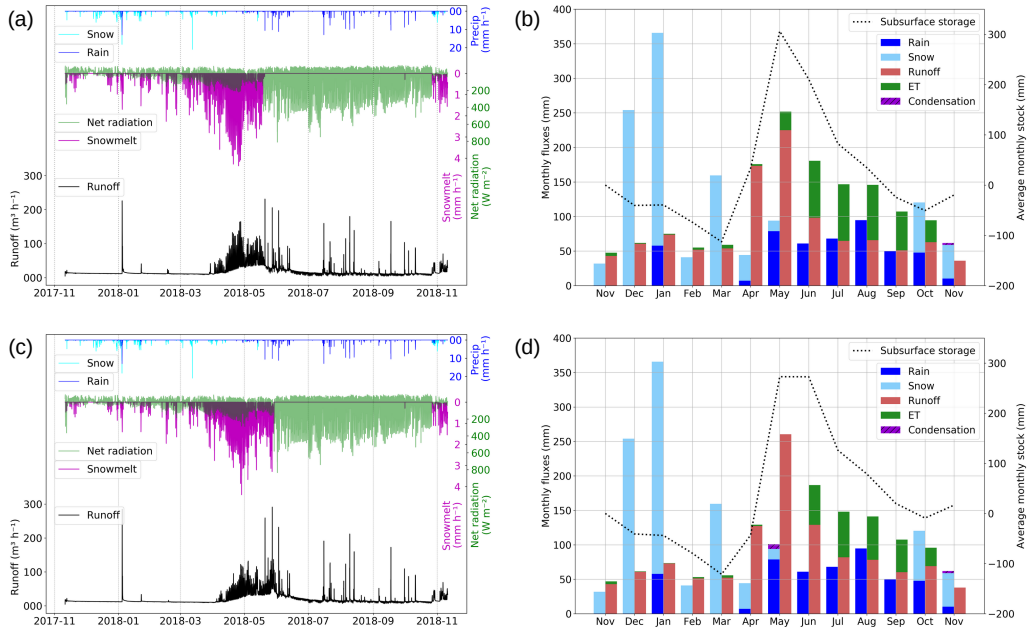


Figure 5. (a) Precipitation (rain – blue and snow – light skyblue), streamflow (black), snowmelt (magenta) and net radiation (green) regimes along the simulation period for only precipitation distributed mean simulation (1D-PM). (b) Monthly water budget for 1D-PM simulation including rain (blue) snow (light skyblue), Runoff (red), ET (green) and condensation (purple). Black dotted line is the total subsurface water storage. (c)(d) same as (a) and (b) but for all distributed mean simulation (1D-AM).

snowmelt in early spring. The factors responsible for this phenomenon include higher sun elevation, clear sky conditions and higher daily temperature.

During winter and spring the monthly cumulated ET is very small (Fig 5b) because of low available energy and complete snow coverage. After the complete snowmelt the model simulates much higher monthly cumulated ET according to the prescribed LAI cycle. ET at this period is higher than the monthly cumulated rain (June, July, September), which means that ET participates in the extraction of shallow water storage during the summer. This can be seen by the difference of subsurface storage decline between the summer (higher water storage diminution) and the winter (lower water storage diminution). In October one can notice a small increase in subsurface storage when ET decreases because of vegetation decay. In the end of the hydrological year, the subsurface water storage has a deficit of 0.15 mm which is much smaller than the annual cycle amplitude.

Figure 5c, d present the same time series and monthly water budgets for the 1D-AM simulation. The major difference compared to 5a, b is that precipitation, solar radiation and wind velocity are prescribed using the spatial average of the distributed field. The major difference comes from solar radiation reduction from 190.8 W m^{-2} to 152.1 W m^{-2} on average which reduces melting and ET. It leads to a 9 days longer snow period, an increased runoff and an increased infiltration of 34.61 mm (Table 2). This unbalance vanishes after 10 years leading to higher water table and then higher runoff with a 0.8 runoff coefficient

when steady state is reached. This means that for similar geomorphology, any reduction in input solar radiation because of catchment orientation or else will lead to higher water table and then higher runoff coefficient.

5.2 Distributed forcing simulations

In the following section, we will discuss the differences in surface hydrological fluxes for all combined and individually distributed simulations, along with their role in streamflow generation.

Looking at the surface fluxes on Fig. 6a, one can see that the simulation with all distributed forcing (2D-AD) have longer snowmelt period with a long steady decline during the streamflow recession till mid-July. Compared to the non-distributed forcing simulation 1D-PM, the distributed forcing is causing a smoother snowmelt dynamic which last till July and correspondingly impacts the net radiation, recharge and streamflow discharge dynamic. It leads to significant differences for streamflow values during the core of the melting period up to 50 % more for 1D-AM compared to 2D-AD. However, budget terms have only 2 % difference at scale of annual water budget between 1D-AM and 2D-AD simulations. From this point of view distribution at that scale seems not to add much information compared to a 1D forcing.

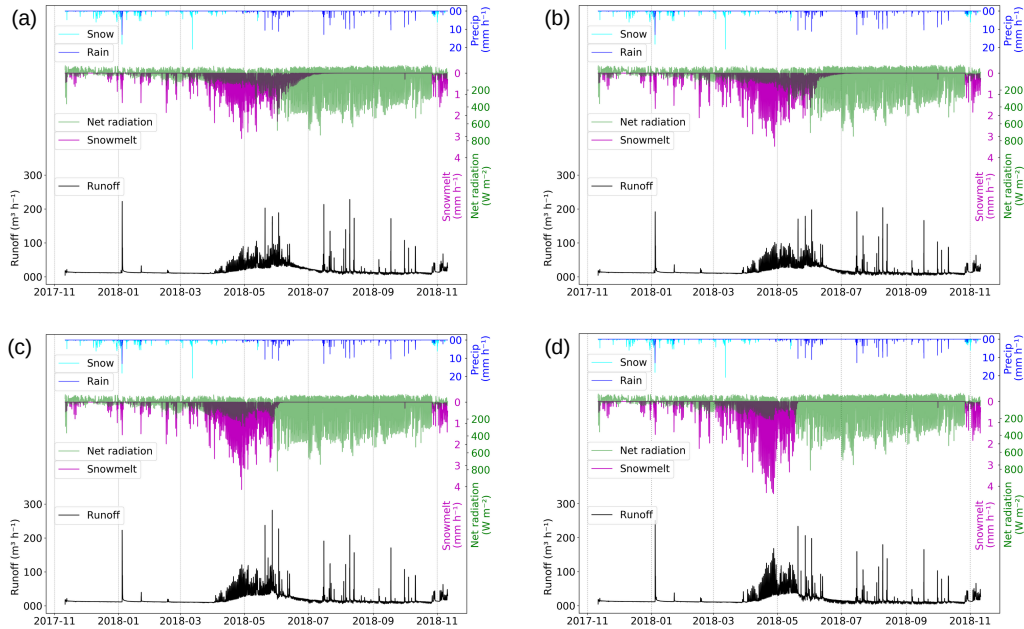


Figure 6. Same figure as 5a for (a) all distributed run (2D-AD), (b) only precipitation distributed run (2D-PD), (c) only shortwave radiation distributed run (2D-SD) and (d) only wind speed distributed run (2D-WD).

Looking at individually distributed simulation results, it seems that this smoothing effect is caused by both the precipitation and shortwave radiation distribution (Fig. 6b, c). At the contrary only wind speed distributed (2D-WD) results seem very similar to the non-distributed results. One can even refer to figure 6d for easier inter-comparison with figure 5a. The melting period tail length seems to be controlled by the snow pack depth variability (Fig. 9a, b) and higher accumulated snow on some

pixels. This is combined with solar radiation effects which also produces spatial variability in snowmelt on the catchment even if the snow precipitation is uniformly distributed (Fig. 6c). Only wind speed distribution (2D-WD) simulation shows the highest melting regimes from mid-March to mid-May when temperature and incoming radiations are favourable for melting with daily melting peaks larger than 4 mm h^{-1} (Fig. 6d). In detail, wind speed distribution shows increase in the melting rate which leads to higher subsurface storage when compared to 1D-PM.

Streamflow differences between simulations basically follow the melting differences. The impact of the late April and early May rain-on-snow period is visible on streamflow on figure 6a, b. It must be noted that there are differences in term of incoming solar radiation between simulations. Unsurprisingly 2D-WD and 2D-PD simulations show larger streamflow values compared to 2D-AD and 2D-SD simulations. This happens because for the former two, the catchment receives 38.7 W m^{-2} less radiation than the latter two. Concerning the summer period when snow gets melted, these differences are not visible on the streamflow.

Figure 7 shows observed and simulated evapotranspiration time series over the two weeks summer window from 08/07 to 25/07 and scatterplots over the two vegetative months from early July to end of August. This is a snow-free period. For better comparison with observations we selected simulated pixels in an approximated footprint area based on a wind direction mask (Fig. 1) and averaged simulated values over the mask (section 3.3). Pixel simulation (Pix-PM) corresponds to the 1D vertical column run at Flux'Alp cell (without lateral flow).

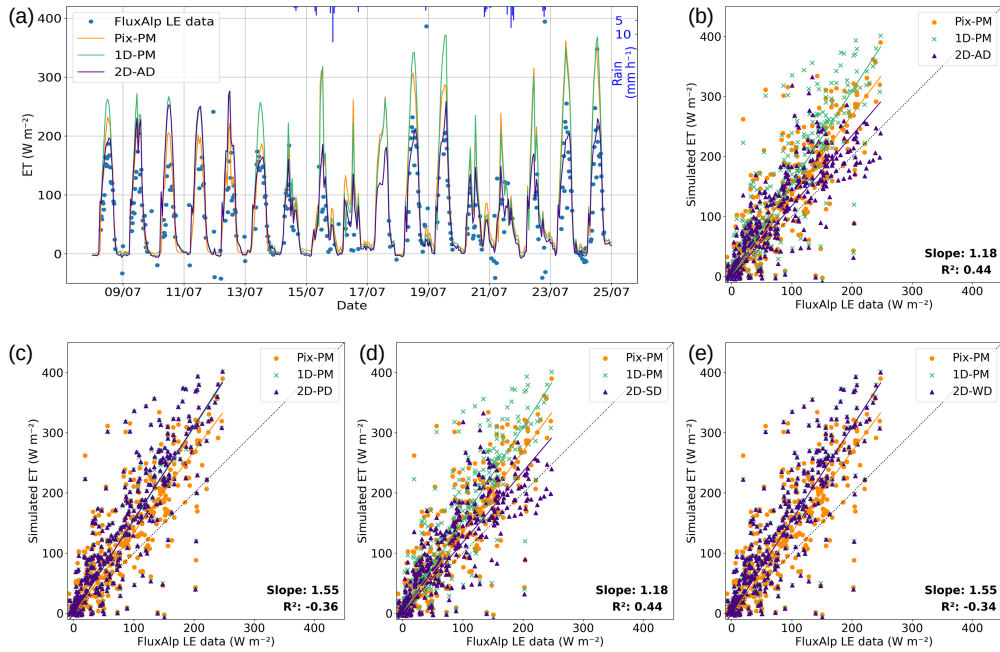


Figure 7. (a) Evapotranspiration simulation masked with wind direction mask for 17 days in summer for all distributed run (2D-AD). Scatter plot for the July-August 2018 period for (b) all distributed run (2D-AD), (c) only precipitation distributed run (2D-PD), (d) only shortwave radiation distributed run (2D-SD) and (e) only wind speed distributed run (2D-WD).

Simulations	Precipitation (mm)	Runoff (mm)	Runof coef. (mm)	ET (mm)	Subsurface storage (mm)
1D-PM	1443.72	1060.74	0.73	372.94	0.15
1D-AM	1443.72	1124.38	0.78	262.77	34.61
2D-AD	1443.72	1097.25	0.77	266.26	32.34
2D-PD	1443.72	1047.83	0.73	361.37	-4.30
2D-SD	1443.72	1098.89	0.76	269.09	33.70
2D-WD	1443.72	1047.94	0.73	371.82	15.50

Table 2. Annual water budget terms in the catchment for different chosen runs.

The pixel run (orange curve and orange dots) clearly overestimated observed evapotranspiration as one can see on both the time series and the scatter plots. This is also the case for the non-distributed simulation (green curve and green dots) and for 2D-PD and 2D-WD which have comparable evapotranspiration amplitude (Fig. 7c, e). However, 2D-AD and 2D-SD have reduced simulated ET which better matches the observations (Fig. 7b, d). This happens because the average shortwave radiation after the distribution is less than the shortwave radiation without distribution (section 4). Also, the catchment is facing east which actually reduces direct incoming solar radiation from noon to sunset.

The evapotranspiration of both Pix-PM and 1D-PM overestimates ET compared to observations. First the pixel run (Pix-PM) is supposed to simulate a catchment border (Flux' Alp location) with dryer soil/ground condition (top of a ridge) and the ET observations are supposed to average both the wet zone close to the river and the dryer zones. However, it is not the case in our pixel and 1D-PM simulations. Shortwave radiation distribution (Fig. 7d) seems to have the most important impact in our measurement area. The corresponding reduced ET in 2D-SD (and 2D-AD), averaged on the footprint area, also corresponds much better to the Eddy-Covariance observations (decrease in regression slope from 1.55 to 1.18).

5.3 Hydrological budget

Annual water budgets (Table 2) shows that the main impact of forcing distribution is caused by the shortwave radiation distribution and subsequent ET calculation. This increases the runoff coefficient from 0.73 to 0.77. One can also note the water storage change over the year. As we started from the same initial conditions for all simulations, it reaches more than 30 mm when SW is reduced (1D-AM, 2D-AD and 2D-SD) and 15.5 mm for 2D-WD simulation. It remains smaller than the ET difference and it minimizes runoff coefficient hence not change our conclusions.

Figure 8 shows monthly water budgets for 2D-AD and individually distributed simulations. Snow precipitation from November to March doesn't infiltrate much to fill up the subsurface storage (dotted line). January rain on snow events slightly reduce the subsurface storage. Very similar runoff values are observed among the different forcing. In contrast, from mid-March to June the subsurface storage is replenished by melting (Fig. 5a, Fig. 6) and runoff increases. The 2D-WD forcing produced the largest values of recharge (430 mm) and the 2D-SD the largest values of streamflow. From May to October, streamflow at the

outlet and ET decreases the subsurface storage. Higher shortwave radiations (2D-PD and 2D-WD) led to longer ET periods. One can finally note that reduction in ET because of vegetation senescence in November leads to increased subsurface storage.

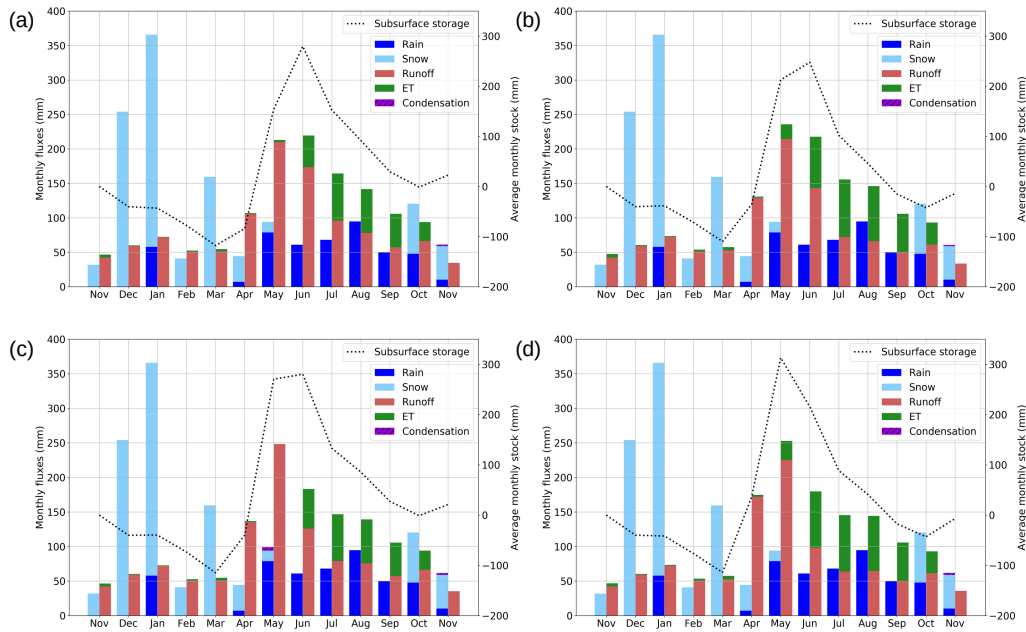


Figure 8. Same figure as 5b for (a) all distributed run (2D-AD), (b) only precipitation distributed run (2D-PD), (c) only shortwave radiation distributed run (2D-SD) and (d) only wind speed distributed run (2D-WD).

5.4 Snow dynamics

Figure 9 shows the temporal dynamics of the snow mantle and the impact in terms of albedo. Snow depth plots for Pix-PM run (purple line) and 1D-PM run (red line) are superimposed. The 1D-PM run shows little variability in snow depth (red shading). These two run follow a dynamic consistent with the observations (black line) and an overestimation along the accumulation period. This is probably because of the rough snow/rain partition temperature threshold and the inability of the snow scheme to account for compaction. The snowmelt dynamic is particularly well simulated (snow cover within the Sentinel-2 image acquisition date), especially along the dry period at the end of April. In early May one can note some discrepancies again probably because of our limited ability to separate rain and snow in the precipitation forcing, close to the phase change temperature range. This can be seen on the pixel simulated Albedo which return to its maximum snow albedo value at the end of the melting season (0.8), which is not the case on the observations. Concerning simulated albedo, it globally follows the observations, however it is clear that the snow age parameterisation in the model is not adequate enough to simulate the albedo where observation shows albedo decrease during melting periods.

In 2D-AD simulation patchiness starts early in May and some snow cover pixels last up to more than one month later compared to the 1D-PM simulation (Fig. 9a). Depth variability increases during snow accumulation events and is slightly

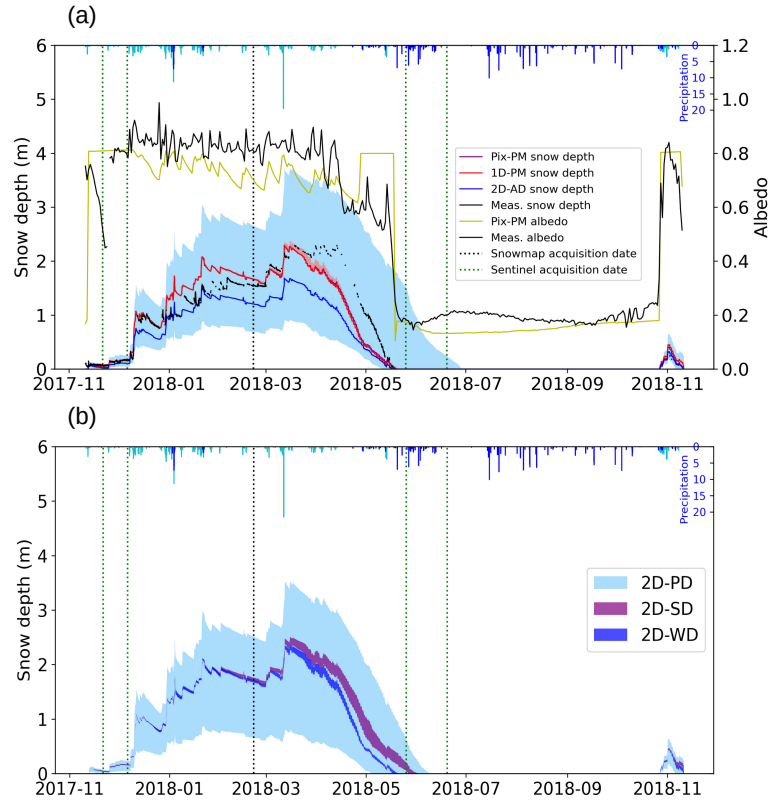


Figure 9. (a) Snow depth (left axis) for different simulations compared with observations (black line). Colour lines are the average depth over the catchment and shadings the spatial variability. Right axis: observed (black line) and 1D-PM simulated albedo (yellow line). Averaged precipitation (rain in blue and snow in cyan) are plotted at the top of the graph. (b) same as (a) but for the only precipitation (2D-PD), only shortwave radiation (2D-SD) and only wind speed (2D-WD) distributed run.

reduced during melting. This effect can also be seen on the 2D-PD simulation but not on any other distributed forcing simulation (Fig. 9b). As 2D-AD and 2D-PD simulations were prescribed the same input precipitation and temperature, this means this effect (the deeper the snow, the faster the melting) is intrinsic to the snow scheme. At the contrary, 2D-SD simulation shows a slight increase of depth variability during the melting period.

It can be observed in figure 9b that none of the individually distributed simulations have longer snow cover compared to the all distributed run (Fig. 9a). It indicates that snow variability during snow accumulation events is not enough to capture the actual behaviour of snow dynamics. The combination of both forcing results in longer snow periods with more patchiness accounting the precipitation spatial variability during accumulation events and the shortwave radiation spatial distribution dominance for differential snow melting. The 2D-WD simulation does not show much impact on the snow depth variability which is very similar to the 1D-PM simulation at the end of the snow period (Fig. 9b). However along spring (mid-March to end of April) it produced the same snow depth spatial variability as 2D-SD and higher snowmelt regimes (Fig. 9b and 6d). Wind

	Satellite platform	Date of acquisition	Resolution (m)	Cloud cover (%)	Cloud cover over catchment (%)
1	Sentinel 2B	2017-11-21	10	1.2	None
2	Sentinel 2A	2017-12-06	10	3.3	None
3	Sentinel 2A	2018-05-25	10	12.8	None
4	Sentinel 2B	2018-06-19	10	2.1	None

Table 3. Images characteristics from ESA’s Sentinel-2 mission.

speed distribution is also impacting snow patchiness through wind transport (accounted in the snow distribution algorithm). In figure 9 the 2D-WD simulation shows small increase in snow variability compared to 1D-PM simulation. However, the wind distribution favours more spatial dynamics when combined with other forcings.

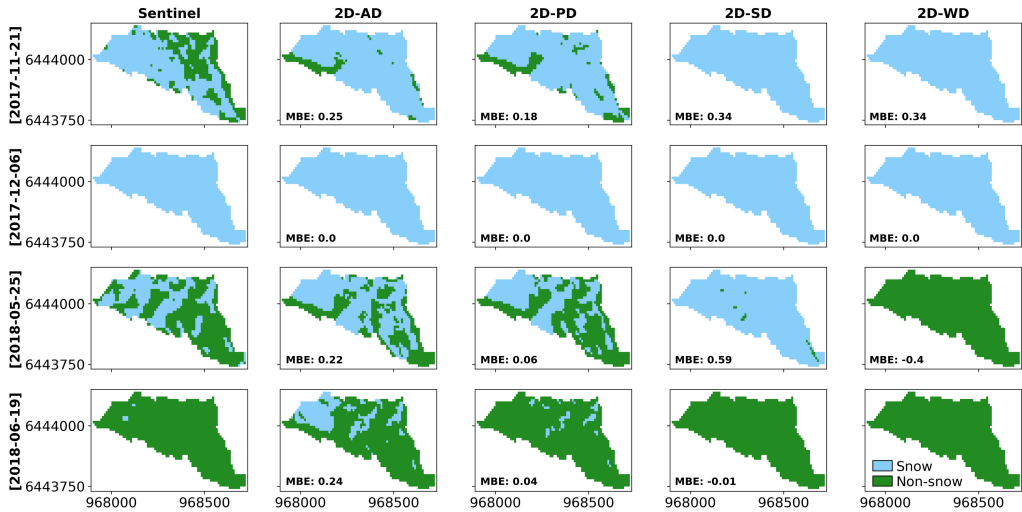


Figure 10. Snow map for different simulations compared with the Sentinel-2 images for 4 cloud free images: snow pixels (light skyblue) and non-snow pixel (green).

Spatial distribution of snow cover during the melting period is shown on figure 10 for all simulations. For comparison and validation, we used four cloud-free ‘Sentinel-2’ images (Table 3). On 21st of November first snow events are followed by a partial melting over the catchment (1st Sentinel-2 image). Our 2D-AD and 2D-PD simulations are partially good in representing this feature, but the simulated melting was overall not enough. It is interesting to see that apart from the upper part of the catchment where snow distribution is not well controlled, the first pixels that get out of snow belongs to the eastern edge of the catchment, a central area aligned with the river left bank and the outlet area. The 2D-AD simulation has less snow cover than 2D-PD because of reduced incoming radiation caused by reduced solar angle which decreases the melting. On 6th of December, the catchment is completely covered by snow for all simulation. It has to be noted that this date corresponds

Variable		Metrics	2D-AD	2D-PD	2D-SD	2D-WD
Evapotranspiration		Slope	1.18	1.55	1.18	1.55
		R-Square	0.44	-0.36	0.44	-0.34
		RMSE	50.77	79.14	50.90	78.41
Albedo		R-Square	0.85	0.88	0.77	0.85
		RMSE	0.12	0.10	0.14	0.12
Snow cover (Sentinel-2)	MBE	21 Nov, 2017	0.25	0.18	0.34	0.34
		06 Dec, 2017	0.00	0.00	0.00	0.00
		25 May, 2018	0.22	0.06	0.59	-0.40
		19 June, 2018	0.24	0.04	-0.01	-0.01
	RMSE	21 Nov, 2017	0.63	0.65	0.58	0.58
		06 Dec, 2017	0.00	0.00	0.00	0.00
		25 May, 2018	0.74	0.75	0.78	0.63
		19 June, 2018	0.50	0.23	0.07	0.07

Table 4. Statistical metrics for observed and simulated parameter among different simulations (MBE: mean bias error, RMSE: root mean square error).

to early season snow events when the 2D-AD and 2D-PD simulations are able to represent the snow dynamic even for very low snow depth. This means in particular that 1) our spinup process has initiated well the ground temperature profile and its distribution and 2) our distribution algorithm is well adapted, especially for snow deposition. On 25th of May the catchment is partially snow covered which is specific to the advancement of melting season. Again 2D-PD simulation represents very well the snow pixels to non-snow pixels ratio and the snow distribution (MBE = 0.06). One can see on both Sentinel-2 image and 2D-PD simulation some SW-NE alignment slightly present on the snow distribution coefficient map (green/blue pixels on Fig. 1c), the timing of disappearance is remarkably well simulated for these pixels. The 2D-AD is not as good (MBE = 0.22) because of more snow cover than the Sentinel-2 image. However, this does not mean that 2D-AD simulation is worse than the 2D-PD. This will be discussed in the next section.

6 Discussion

The presented simulations disentangle the combined effects of snow and solar radiation distributions. This make us able to simulate realistic patchy snow cover at 10 m resolution (Fig. 10) which is a commonly observed phenomenon over mid altitude mountainous catchment (Revuelto et al., 2020). The all distributed simulation (2D-AD), which encapsulate snow distribution based on snowmap and shortwave radiation distribution based on slope, efficiently simulates these characteristics in our test case. However, 2D-AD simulation is not the best one in term of spatial melting. The reduction in melt when solar incidence is taken into account, this simulation lags the complete melt by ~20 days (Fig. 9). However, we have already shown the capability

425 of 2D-AD simulation in capturing the better ET dynamics as compared to 2D-PD simulation(Fig. 7b, d). Looking at the laser scan date, it shows a ~ 0.5 m difference between the snow accumulation and the laser scan. One reason could be that the snow distribution coefficient map we used slightly overestimated the distributed amount of snow. Another reason could be the albedo scheme. The unusual shoot-up of albedo in April leads to a decrease in melting and subsequently higher snow depth distribution in the catchment. If we assume this to be true, then 2D-AD will be the best simulation in term of spatial snow melting.

430 The results show the large sensitivity of Evapotranspiration to incoming solar radiation corrections (decrease in regression slope from 1.55 to 1.18). In the presented results, evapotranspiration spatial average remains larger than observations. The reason to overestimate the evapotranspiration could come from our footprint area (Oishi et al., 2008). We choose a very simple approach to consider large heterogeneity (moisture, vegetation) in the ET observation footprint which consists in the presented wind direction mask (Fig. 1). We hypothesise this spatial average is better than a single pixel to compare simulated
435 evapotranspiration series with observations. The micro-topography of the catchment is undulating, which induces moisture heterogeneity with some wetlands in the lowlands. Our footprint area is not as good as in representing the actual footprint area which could also lead to small differences with what we presented. Footprint area calculation from Eddypro (Kljun et al., 2004) gives an average peak distance of ~ 70 m and a 90 % contribution distance of ~ 400 m for summer months daily hours. These distances are larger than the catchment width in the upwind direction. Moreover, footprint area calculation is not easy on such
440 mountainous terrain. The theoretical background of footprint calculation suppose a flat terrain with a fully developed surface layer. This is not the case in our context. For these reasons we choose to keep a simpler approach for a first order estimation of model performance.

ParFLOW-CLM is a critical zone physically based model built to be very close to the hydrological processes (Kuffour et al., 2020; Tran et al., 2020). This requires reliable data for forcing, ground, vegetation and hydrology to keep consistency in the
445 model framework to simulate all water path with the same accuracy. We then chose to work only with local observations from which we built distributed forcing based on presented algorithm and from which we evaluated the model (Liston and Elder, 2006). The model calibration itself consist in building the model, which means underground geometry and parameters from observation are only used. As we don't have observations for each pixels, we built the model on assumptions by supposing that what we measure is also valid for places where we do not have observations. Available observations then restrict ranges to
450 tune the model once we consider embedded parameterisation, which explicitly solves melting and evapotranspiration following basic physical laws. Then we force the model with reliable observed meteorological data. From this approach we can clearly see the importance of snow processes and the role of incoming radiation distributions. Indeed the model has been evaluated against the radiation budget observation (albedo), energy budget observation (latent and sensible heat fluxes), water budget terms including snow cover, ability of the model to produce baseflow and snowmelt timing (Table 4). Validation with Sentinel-
455 2 images during accumulation and melting period shows that simulations are very close to the observation in terms of onset and offset of snowmelt. Spatial distribution of snow is also reported very close to the satellite observation when slope effect are considered in precipitation and solar radiation forcing.

A Last remark about model configuration is that the domain has a no-flow boundary condition on the sides and at the bottom of the domain. ET and streamflow outlet are then the only way to get the water out. In other words, this means that we are

not simulating larger scale flow path (water that enters from the sides of the domain or that gets out through the bottom of the domain) which is probable for high altitudinal mountainous catchments. We started some particle tracking calculations from 3D velocity fields produced by parflow for our simulations. They show very weak percolation and transfers to deep horizons. Most of the water transfers occur in the first 10 m. This subsurface water transfer could also lead to small differences in outlet and evapotranspiration partitioning but it will not change the conclusions of this study.

Fan et al. (2019) highlighted the inclusion of two main processes to account for in the ESMs which includes the slope/aspect effect and soil depth. Our study contribute to this identified issue along with algorithm to take into account surface heterogeneity. In this study we precise how slope/aspect impact hydrological budget given spatial variability in meteorological forcing along with surface to subsurface transfers and how it can be successfully included in critical zone hydrological modeling. The adopted algorithm efficiently captures the surface heterogeneity in the snowcover and evapotranspiration. The same algorithm also influences the temporal distribution of snowmelt and water balance. This highlights the importance of slope, aspect and curvature inclusion in the hydrological studies.

7 Conclusions

Earth system models are gaining ample highlight in socio-economic impact studies. They include more and more processes including the complete continental water cycle but still face difficulty to parameterize small scale sub-mesh processes. **These processes** are crucial in mountain landscapes both for surface hydrology and feedbacks on climate. In this study we modelled the spatial variability of the **snow cover** over a small mid-altitude catchment and its impact on the hydrological budget using the 3D critical-zone model ParFlow-CLM at 10 m resolution. For this purpose, we prepared distributed forcing for precipitation (that include snow transport), incoming solar radiation (that include differential snow melting) and wind speed to force the model. We have shown that the snow lasts longer for more than a month in our modeling setup when distributing all forcings together compared to non-distributed forcing. **These longer snow stays lead to increase in streamflow, subsurface water storage and runoff coefficients but decrease in evapotranspiration because of shorter vegetation periods.** We have shown that the precipitation distribution has a largest impact on hydrological behaviour **because it favours the appearance of snow patches during the melting season. Shortwave radiation** distribution has a smaller effect at creating snow patches in our simulation but enhances the **differential snow melting** when combined with precipitation distribution. Our **wind speed** distributed simulation also induces melting spatial variability in the core of the melting period but **reduces** at the end of the melting period, as only taken into account for evapotranspiration processes. However, wind has a major role on snow re-distribution. This is well accounted in our precipitation distribution algorithm using a laser scan of the snow mantle during the accumulation period which registered the snow variability aligned with the prevailing wind direction. **Furthermore, accounting for distributed solar incidence reduces the incoming radiation in our catchment which subsequently reduces the evapotranspiration.** This led to higher runoff coefficients at catchment scale. In conclusion, this study shows the relative importance of small-scale processes in earth system models when run at hyper-resolution. The terrain substantially controls the hydrological behaviour over the

mid-elevation alpine catchment for runoff generation, evapotranspiration and snow dynamics, which has to be accounted using terrain based meteorologic forcing distribution. It will help to minimise the erratum in water resource management.

The major conclusions of study could be summarised as:

- 495 – Most of hydrological processes are slope dependant but it is merely taken into account in land surface and hydrological models. The study quantifies the hydrological impacts in term of melting, streamflow and evapotranspiration dynamic when taking into account, or not, the slope effect. Considering critical zone models applied to mountainous area, we believe that it is mandatory to consider sub-grid-scale slope/aspect effects in large scale models especially when they are used for hydrological studies.
- 500 – Solar radiation angle with respect to catchment slope is the second most impacting topographic parametrization for melting as well as for evapotranspiration.

Code and data availability. The DOI of published datasets will be made available, which includes the ParFLOW version used in the study, forcing datasets for the non-distributed and all-distributed forcing, input and TCL script to launch ParFLOW. The source code for the ParFLOW version used in this study is available to clone from: (<https://github.com/aniketgupta2009/treeac-alp-parflow-ver-meteo.git>).

505 *Author contributions.* A. Gupta, A. Reverdy, J-M. Cohard, designed the experiments and prepared all the necessary inputs to run the model, and A. Gupta performed the simulations. R. Maxwell and B. Hector developed the model Parflow/CLM Model version for this study, D. Voisin processed required meteorological data, M. Descloîtres and J-P. Vandervaere provided soil and aquifer properties, C. Coulaud, L. Liger and R. Biron manage Eddy Covariance micro-meteorological station and all field works at Lautaret Pass, J-G. Valay and D. Voisin brings the necessary support to make this study possible. A. Gupta and J-M. Cohard prepared the manuscript with contributions from all
510 co-authors.

Competing interests. The authors declare that they have no conflict of interest.

Acknowledgements. This research was conducted within the Long-Term Socio-Ecological Research (LTSER) platform Lautaret-Oisans, a site of the European Research Infrastructure eLTER. It received funding from the Lautaret Garden (Univ. Grenoble Alpes, CNRS, LAUTARET, 38000 Grenoble, France), a member of the Zone Atelier Alpes and the eLTER network and from ANR project ANR-15-
515 IDEX-02.

References

- Aguayo, M. A., Flores, A. N., McNamara, J. P., Marshall, H.-P., and Mead, J.: Examining cross-scale influences of forcing resolutions in a hillslope-resolving, integrated hydrologic model, *Hydrology and Earth System Sciences Discussions*, pp. 1–28, <https://doi.org/https://doi.org/10.5194/hess-2020-451>, publisher: Copernicus GmbH, 2020.
- 520 Ashby, S. F. and Falgout, R. D.: A parallel multigrid preconditioned conjugate gradient algorithm for groundwater flow simulations, *Nuclear science and engineering*, 124, 145–159, iSBN: 0029-5639 Publisher: Taylor & Francis, 1996.
- Baba, M. W., Gascoin, S., Kinnard, C., Marchane, A., and Hanich, L.: Effect of Digital Elevation Model Resolution on the Simulation of the Snow Cover Evolution in the High Atlas, *Water Resources Research*, 55, 5360–5378, <https://doi.org/https://doi.org/10.1029/2018WR023789>, _eprint: <https://onlinelibrary.wiley.com/doi/pdf/10.1029/2018WR023789>, 2019.
- 525 Bertoldi, G., Della Chiesa, S., Notarnicola, C., Pasolli, L., Niedrist, G., and Tappeiner, U.: Estimation of soil moisture patterns in mountain grasslands by means of SAR RADARSAT2 images and hydrological modeling, *Journal of Hydrology*, 516, 245–257, <https://doi.org/10.1016/j.jhydrol.2014.02.018>, 2014.
- Blöschl, G., Bierkens, M. F. P., Chambel, A., Cudennec, C., Destouni, G., Fiori, A., Kirchner, J. W., McDonnell, J. J., Savenije, H. H. G., Sivapalan, M., Stumpp, C., Toth, E., Volpi, E., Carr, G., Lupton, C., Salinas, J., Széles, B., Viglione, A., Aksoy, H., Allen, S. T., Amin, A., Andréassian, V., Arheimer, B., Aryal, S. K., Baker, V., Bardsley, E., Barendrecht, M. H., Bartosova, A., Batelaan, O., Berghuijs, W. R., Beven, K., Blume, T., Bogaard, T., Amorim, P. B. d., Böttcher, M. E., Boulet, G., Breinl, K., Brilly, M., Brocca, L., Buytaert, W., Castellarin, A., Castelletti, A., Chen, X., Chen, Y., Chen, Y., Chiffard, P., Claps, P., Clark, M. P., Collins, A. L., Croke, B., Dathe, A., David, P. C., Barros, F. P. J. d., Rooij, G. d., Baldassarre, G. D., Driscoll, J. M., Duethmann, D., Dwivedi, R., Eris, E., Farmer, W. H., Feicabrino, J., Ferguson, G., Ferrari, E., Ferraris, S., Fersch, B., Finger, D., Foglia, L., Fowler, K., Gartsman, B., Gascoin, S., Gaume, E., Gelfan, A., Geris, J., Gharari, S., Gleeson, T., Glendell, M., Bevacqua, A. G., González-Dugo, M. P., Grimaldi, S., Gupta, A. B., Guse, B., Han, D., Hannah, D., Harpold, A., Haun, S., Heal, K., Helfricht, K., Herrnegger, M., Hipsey, M., Hlaváčiková, H., Hohmann, C., Holko, L., Hopkinson, C., Hrachowitz, M., Illangasekare, T. H., Inam, A., Innocente, C., Istanbuloglu, E., Jarihani, B., Kalantari, Z., Kalvans, A., Khanal, S., Khatami, S., Kiesel, J., Kirkby, M., Knoben, W., Kochanek, K., Kohnová, S., Kolehkina, A., Krause, S., Creamer, D., Kreibich, H., Kunstmann, H., Lange, H., Liberato, M. L. R., Lindquist, E., Link, T., Liu, J., Loucks, D. P., Luce, C., Mahé, G., Makarieva, O., Malard, J., Mashtayeva, S., Maskey, S., Mas-Pla, J., Mavrova-Guirguinova, M., Mazzoleni, M., Mernild, S., Misstear, B. D., Montanari, A., Müller-Thomy, H., Nabizadeh, A., Nardi, F., Neale, C., Nesterova, N., Nurtaev, B., Odongo, V. O., Panda, S., Pande, S., Pang, Z., Papacharalampous, G., Perrin, C., Pfister, L., Pimentel, R., Polo, M. J., Post, D., Sierra, C. P., Ramos, M.-H., Renner, M., Reynolds, J. E., Ridolfi, E., Rigon, R., Riva, M., Robertson, D. E., Rosso, R., Roy, T., Sá, J. H. M., Salvadori, G., Sandells, M., Schaeffli, B., Schumann, A., Scolobig, A., Seibert, J., Servat, E., Shafiei, M., Sharma, A., Sidibe, M., Sidle, R. C., Skaugen, T., Smith, H., Spiessl, S. M., Stein, L., Steinsland, I., Strasser, U., Su, B., Szolgay, J., Tarboton, D., Tauro, F., Thirel, G., Tian, F., Tong, R., Tussupova, K., Tyralis, H., Uijlenhoet, R., Beek, R. v., Ent, R. J. v. d., Ploeg, M. v. d., Loon, A. F. V., Meerveld, I. v., Nooijen, R. v., Oel, P. R. v., Vidal, J.-P., Freyberg, J. v., Vorogushyn, S., Wachniew, P., Wade, A. J., Ward, P., Westerberg, I. K., White, C., Wood, E. F., Woods, R., Xu, Z., Yilmaz, K. K., and Zhang, Y.: Twenty-three unsolved problems in hydrology (UPH) – a community perspective, *Hydrological Sciences Journal*, 64, 1141–1158, <https://doi.org/10.1080/02626667.2019.1620507>, publisher: Taylor & Francis _eprint: <https://doi.org/10.1080/02626667.2019.1620507>, 2019.
- 550 Brutsaert, W.: The surface roughness parameterization, in: *Evaporation into the Atmosphere*, pp. 113–127, Springer, 1982.

- Clark, M. P., Fan, Y., Lawrence, D. M., Adam, J. C., Bolster, D., Gochis, D. J., Hooper, R. P., Kumar, M., Leung, L. R., Mackay, D. S., Maxwell, R. M., Shen, C., Swenson, S. C., and Zeng, X.: Improving the representation of hydrologic processes in Earth System Models, *Water Resources Research*, 51, 5929–5956, <https://doi.org/https://doi.org/10.1002/2015WR017096>, _eprint: <https://onlinelibrary.wiley.com/doi/pdf/10.1002/2015WR017096>, 2015.
- Condon, L. E. and Maxwell, R. M.: Modified priority flood and global slope enforcement algorithm for topographic processing in physically based hydrologic modeling applications, *Computers & Geosciences*, 126, 73–83, <https://doi.org/10.1016/j.cageo.2019.01.020>, 2019.
- Costa, D., Shook, K., Spence, C., Elliott, J., Baulch, H., Wilson, H., and Pomeroy, J. W.: Predicting Variable Contributing Areas, Hydrological Connectivity, and Solute Transport Pathways for a Canadian Prairie Basin, *Water Resources Research*, 56, e2020WR027984, <https://doi.org/10.1029/2020WR027984>, publisher: John Wiley & Sons, Ltd, 2020.
- Dai, Y., Zeng, X., Dickinson, R. E., Baker, I., Bonan, G. B., Bosilovich, M. G., Denning, A. S., Dirmeyer, P. A., Houser, P. R., Niu, G., Oleson, K. W., Schlosser, C. A., and Yang, Z.-L.: The Common Land Model, *Bulletin of the American Meteorological Society*, 84, 1013–1024, <https://doi.org/10.1175/BAMS-84-8-1013>, publisher: American Meteorological Society Section: Bulletin of the American Meteorological Society, 2003.
- Dozier, J.: Spectral signature of alpine snow cover from the Landsat Thematic Mapper, *Remote sensing of environment*, 28, 9–22, ISBN: 0034-4257 Publisher: Elsevier, 1989.
- Drusch, M., Del Bello, U., Carlier, S., Colin, O., Fernandez, V., Gascon, F., Hoersch, B., Isola, C., Laberinti, P., and Martimort, P.: Sentinel-2: ESA’s optical high-resolution mission for GMES operational services, *Remote sensing of Environment*, 120, 25–36, ISBN: 0034-4257 Publisher: Elsevier, 2012.
- Dunne, T.: Relation of field studies and modeling in the prediction of storm runoff, *Journal of Hydrology*, 65, 25–48, [https://doi.org/10.1016/0022-1694\(83\)90209-3](https://doi.org/10.1016/0022-1694(83)90209-3), 1983.
- Fan, Y., Clark, M., Lawrence, D. M., Swenson, S., Band, L. E., Brantley, S. L., Brooks, P. D., Dietrich, W. E., Flores, A., Grant, G., Kirchner, J. W., Mackay, D. S., McDonnell, J. J., Milly, P. C. D., Sullivan, P. L., Tague, C., Ajami, H., Chaney, N., Hartmann, A., Hazenberg, P., McNamara, J., Pelletier, J., Perket, J., Rouholahnejad-Freund, E., Wagener, T., Zeng, X., Beighley, E., Buzan, J., Huang, M., Livneh, B., Mohanty, B. P., Nijssen, B., Safeeq, M., Shen, C., Verseveld, W. v., Volk, J., and Yamazaki, D.: Hillslope Hydrology in Global Change Research and Earth System Modeling, *Water Resources Research*, 55, 1737–1772, <https://doi.org/https://doi.org/10.1029/2018WR023903>, _eprint: <https://onlinelibrary.wiley.com/doi/pdf/10.1029/2018WR023903>, 2019.
- Fang, X. and Pomeroy, J. W.: Diagnosis of future changes in hydrology for a Canadian Rockies headwater basin, *Hydrology and Earth System Sciences*, 24, 2731–2754, <https://doi.org/https://doi.org/10.5194/hess-24-2731-2020>, publisher: Copernicus GmbH, 2020.
- Günther, D., Marke, T., Essery, R., and Strasser, U.: Uncertainties in Snowpack Simulations—Assessing the Impact of Model Structure, Parameter Choice, and Forcing Data Error on Point-Scale Energy Balance Snow Model Performance, *Water Resources Research*, 55, 2779–2800, <https://doi.org/https://doi.org/10.1029/2018WR023403>, _eprint: <https://onlinelibrary.wiley.com/doi/pdf/10.1029/2018WR023403>, 2019.
- Hellström, M., Vermeulen, A., Mirzov, O., Sabbatini, S., Vitale, D., Papale, D., Tarniewicz, J., Hazan, L., Rivier, L., and Jones, S. D.: Near Real Time Data Processing In ICOS RI, in: 2nd international workshop on interoperable infrastructures for interdisciplinary big data sciences (it4ris 16) in the context of ieee real-time system symposium (rtss), 2016.
- Horton, R. E.: The Rôle of infiltration in the hydrologic cycle, *Eos, Transactions American Geophysical Union*, 14, 446–460, <https://doi.org/https://doi.org/10.1029/TR014i001p00446>, _eprint: <https://onlinelibrary.wiley.com/doi/pdf/10.1029/TR014i001p00446>, 1933.

- 590 Hurrell, J. W., Holland, M. M., Gent, P. R., Ghan, S., Kay, J. E., Kushner, P. J., Lamarque, J.-F., Large, W. G., Lawrence, D., Lindsay, K., Lipscomb, W. H., Long, M. C., Mahowald, N., Marsh, D. R., Neale, R. B., Rasch, P., Vavrus, S., Vertenstein, M., Bader, D., Collins, W. D., Hack, J. J., Kiehl, J., and Marshall, S.: The Community Earth System Model: A Framework for Collaborative Research, *Bulletin of the American Meteorological Society*, 94, 1339–1360, <https://doi.org/10.1175/BAMS-D-12-00121.1>, publisher: American Meteorological Society Section: Bulletin of the American Meteorological Society, 2013.
- 595 Jefferson, J. L. and Maxwell, R. M.: Evaluation of simple to complex parameterizations of bare ground evaporation, *Journal of Advances in Modeling Earth Systems*, 7, 1075–1092, <https://doi.org/https://doi.org/10.1002/2014MS000398>, _eprint: <https://onlinelibrary.wiley.com/doi/pdf/10.1002/2014MS000398>, 2015.
- Jones, J. E. and Woodward, C. S.: Newton–Krylov-multigrid solvers for large-scale, highly heterogeneous, variably saturated flow problems, *Advances in Water Resources*, 24, 763–774, iSBN: 0309-1708 Publisher: Elsevier, 2001.
- 600 Kljun, N., Calanca, P., Rotach, M. W., and Schmid, H. P.: A simple parameterisation for flux footprint predictions, *Boundary-Layer Meteorology*, 112, 503–523, iSBN: 1573-1472 Publisher: Springer, 2004.
- Klok, E. J., Jasper, K., Roelofsma, K. P., Gurtz, J., and Badoux, A.: Distributed hydrological modelling of a heavily glaciated Alpine river basin, *Hydrological sciences journal*, 46, 553–570, iSBN: 0262-6667 Publisher: Taylor & Francis, 2001.
- Kollet, S. J. and Maxwell, R. M.: Integrated surface–groundwater flow modeling: A free-surface overland flow boundary condition in a parallel groundwater flow model, *Advances in Water Resources*, 29, 945–958, <https://doi.org/10.1016/j.advwatres.2005.08.006>, 2006.
- 605 Kollet, S. J. and Maxwell, R. M.: Capturing the influence of groundwater dynamics on land surface processes using an integrated, distributed watershed model, *Water Resources Research*, 44, <https://doi.org/https://doi.org/10.1029/2007WR006004>, _eprint: <https://onlinelibrary.wiley.com/doi/pdf/10.1029/2007WR006004>, 2008.
- Kuffour, B. N. O., Engdahl, N. B., Woodward, C. S., Condon, L. E., Kollet, S., and Maxwell, R. M.: Simulating coupled surface–subsurface flows with ParFlow v3.5.0: capabilities, applications, and ongoing development of an open-source, massively parallel, integrated hydrologic model, *Geoscientific Model Development*, 13, 1373–1397, <https://doi.org/https://doi.org/10.5194/gmd-13-1373-2020>, publisher: Copernicus GmbH, 2020.
- 610 Liston, G. E. and Elder, K.: A Meteorological Distribution System for High-Resolution Terrestrial Modeling (MicroMet), *Journal of Hydrometeorology*, 7, 217–234, <https://doi.org/10.1175/JHM486.1>, publisher: American Meteorological Society Section: Journal of Hydrometeorology, 2006.
- 615 Liston, G. E., Perham, C. J., Shideler, R. T., and Cheuvront, A. N.: Modeling snowdrift habitat for polar bear dens, *Ecological Modelling*, 320, 114–134, <https://doi.org/10.1016/j.ecolmodel.2015.09.010>, 2016.
- Loritz, R., Hrachowitz, M., Neuper, M., and Zehe, E.: The role and value of distributed precipitation data in hydrological models, *Hydrology and Earth System Sciences*, 25, 147–167, <https://doi.org/https://doi.org/10.5194/hess-25-147-2021>, publisher: Copernicus GmbH, 2021.
- 620 Marsh, C. B., Pomeroy, J. W., Spiteri, R. J., and Wheeler, H. S.: A Finite Volume Blowing Snow Model for Use With Variable Resolution Meshes, *Water Resources Research*, 56, e2019WR025 307, <https://doi.org/https://doi.org/10.1029/2019WR025307>, _eprint: <https://onlinelibrary.wiley.com/doi/pdf/10.1029/2019WR025307>, 2020.
- Maxwell, R. M.: A terrain-following grid transform and preconditioner for parallel, large-scale, integrated hydrologic modeling, *Advances in Water Resources*, 53, 109–117, iSBN: 0309-1708 Publisher: Elsevier, 2013.
- 625 Maxwell, R. M. and Miller, N. L.: Development of a coupled land surface and groundwater model, *Journal of Hydrometeorology*, 6, 233–247, iSBN: 1525-7541, 2005.

- Meerveld, H. J. T.-v., James, A. L., McDonnell, J. J., and Peters, N. E.: A reference data set of hillslope rainfall-runoff response, Panola Mountain Research Watershed, United States, Water Resources Research, 44, <https://doi.org/https://doi.org/10.1029/2007WR006299>, _eprint: <https://onlinelibrary.wiley.com/doi/pdf/10.1029/2007WR006299>, 2008.
- 630 Nijssen, B. and Lettenmaier, D. P.: A simplified approach for predicting shortwave radiation transfer through boreal forest canopies, Journal of Geophysical Research: Atmospheres, 104, 27 859–27 868, <https://doi.org/https://doi.org/10.1029/1999JD900377>, _eprint: <https://onlinelibrary.wiley.com/doi/pdf/10.1029/1999JD900377>, 1999.
- Oishi, A. C., Oren, R., and Stoy, P. C.: Estimating components of forest evapotranspiration: a footprint approach for scaling sap flux measurements, agricultural and forest meteorology, 148, 1719–1732, iSBN: 0168-1923 Publisher: Elsevier, 2008.
- 635 Oleson, K. W., Dai, Y., Bonan, G., Bosilovich, M., Dickinson, R., Dirmeyer, P., Hoffman, F., Houser, P., Levis, S., and Niu, G.-Y.: Technical description of the community land model (CLM), Tech. Note NCAR/TN-461+ STR, 2004.
- Pomeroy, J. W. and Li, L.: Prairie and arctic areal snow cover mass balance using a blowing snow model, Journal of Geophysical Research: Atmospheres, 105, 26 619–26 634, <https://doi.org/https://doi.org/10.1029/2000JD900149>, _eprint: <https://onlinelibrary.wiley.com/doi/pdf/10.1029/2000JD900149>, 2000.
- 640 Pomeroy, J. W., Toth, B., Granger, R. J., Hedstrom, N. R., and Essery, R. L. H.: Variation in Surface Energetics during Snowmelt in a Subarctic Mountain Catchment, Journal of Hydrometeorology, 4, 702–719, [https://doi.org/10.1175/1525-7541\(2003\)004<0702:VISED>2.0.CO;2](https://doi.org/10.1175/1525-7541(2003)004<0702:VISED>2.0.CO;2), publisher: American Meteorological Society Section: Journal of Hydrometeorology, 2003.
- Pomeroy, J. W., Gray, D. M., Brown, T., Hedstrom, N. R., Quinton, W. L., Granger, R. J., and Carey, S. K.: The cold regions hydrological model: a platform for basing process representation and model structure on physical evidence, Hydrological Processes, 21, 2650–2667, <https://doi.org/https://doi.org/10.1002/hyp.6787>, _eprint: <https://onlinelibrary.wiley.com/doi/pdf/10.1002/hyp.6787>, 2007.
- 645 Revuelto, J., Azorin-Molina, C., Alonso-González, E., Sanmiguel-Valladolid, A., Navarro-Serrano, F., Rico, I., and López-Moreno, J. I.: Meteorological and snow distribution data in the Izas Experimental Catchment (Spanish Pyrenees) from 2011 to 2017, Earth System Science Data, 9, 993–1005, <https://doi.org/https://doi.org/10.5194/essd-9-993-2017>, publisher: Copernicus GmbH, 2017.
- Revuelto, J., Billecocq, P., Tuzet, F., Cluzet, B., Lamare, M., Larue, F., and Dumont, M.: Random forests as a tool to understand the snow depth distribution and its evolution in mountain areas, Hydrological Processes, 34, 5384–5401, <https://doi.org/https://doi.org/10.1002/hyp.13951>, _eprint: <https://onlinelibrary.wiley.com/doi/pdf/10.1002/hyp.13951>, 2020.
- 650 Riggs, G., Hall, D., and Salomonson, V.: A snow index for the Landsat Thematic Mapper and Moderate Resolution Imaging Spectroradiometer, in: Proceedings of IGARSS '94 - 1994 IEEE International Geoscience and Remote Sensing Symposium, vol. 4, pp. 1942–1944 vol.4, <https://doi.org/10.1109/IGARSS.1994.399618>, 1994.
- 655 Sampaio, R. J., Rodriguez, D. A., Von Randow, C., da Silva, F. P., de Araújo, A. A. M., and Filho, O. C. R.: Sensible heat flux assessment in a complex coastal-mountain urban area in the metropolitan area of Rio de Janeiro, Brazil, Meteorology and Atmospheric Physics, <https://doi.org/10.1007/s00703-021-00812-2>, 2021.
- Sevruk, B. and WMO, G.: Correction of precipitation measurements.(Proceedings), publisher: Zuerich (Switzerland) ETH, Geographisches Inst., 1986.
- 660 Song, J., Miller, G. R., Cahill, A. T., Aparecido, L. M. T., and Moore, G. W.: Modeling land surface processes over a mountainous rainforest in Costa Rica using CLM4.5 and CLM5, Geoscientific Model Development, 13, 5147–5173, <https://doi.org/https://doi.org/10.5194/gmd-13-5147-2020>, publisher: Copernicus GmbH, 2020.

- Sun, N., Wigmosta, M., Zhou, T., Lundquist, J., Dickerson-Lange, S., and Cristea, N.: Evaluating the functionality and streamflow impacts of explicitly modelling forest–snow interactions and canopy gaps in a distributed hydrologic model, *Hydrological Processes*, 32, 2128–2140, <https://doi.org/10.1002/hyp.13150>, _eprint: <https://onlinelibrary.wiley.com/doi/pdf/10.1002/hyp.13150>, 2018.
- Tran, H., Zhang, J., Cohard, J.-M., Condon, L. E., and Maxwell, R. M.: Simulating Groundwater-Streamflow Connections in the Upper Colorado River Basin, *Groundwater*, 58, 392–405, <https://doi.org/https://doi.org/10.1111/gwat.13000>, _eprint: <https://onlinelibrary.wiley.com/doi/pdf/10.1111/gwat.13000>, 2020.
- van den Hurk, B., Best, M., Dirmeyer, P., Pitman, A., Polcher, J., and Santanello, J.: Acceleration of land surface model development over a decade of GLASS, *Bulletin of the American Meteorological Society*, 92, 1593–1600, iSBN: 0003-0007 Publisher: JSTOR, 2011.
- Van Genuchten, M. T.: A closed-form equation for predicting the hydraulic conductivity of unsaturated soils, *Soil science society of America journal*, 44, 892–898, iSBN: 0361-5995 Publisher: Wiley Online Library, 1980.
- Vionnet, V., Brun, E., Morin, S., Boone, A., Faroux, S., Le Moigne, P., Martin, E., and Willemet, J.-M.: The detailed snowpack scheme Crocus and its implementation in SURFEX v7.2, *Geoscientific Model Development*, 5, 773–791, <https://doi.org/10.5194/gmd-5-773-2012>, 2012.